PERGAMON

Continental Shelf Research 19 (1999) 271–288

CONTINENTAL SHELF RESEARCH

An EOF analysis of HF Doppler radar current measurements of the Chesapeake Bay buoyant outflow

G.O. Marmorino[a,*], L.K. Shay[b], B.K. Haus[b], R.A. Handler[a], H.C. Graber[b], M.P. Horne[a]

[a] *Remote Sensing Division, Naval Research Laboratory, Code 7250, Washington DC 20375-5357, USA*
[b] *Rosenstiel School of Marine and Atmospheric Science, University of Miami, USA*

Received 16 March 1998; accepted 21 July 1998

Abstract

Surface currents measured by HF Doppler radar as part of a study of the Chesapeake Bay outflow plume are examined using a 'real-vector' empirical orthogonal function (EOF) analysis (Kaihatu et al., 1998). Based on about 23 days of nearly continuous data, the analysis shows that the first three EOF modes, judged to be the only significant modes, account for 76% of the variance in the data set. The buoyant outflow occurs primarily in the mean flow field. The first EOF mode is dominated by wind forcing and the second mode by across-shelf semi-diurnal tidal forcing. The third mode exhibits a large-scale horizontal shear and contains a curved region of weak relative flow which appears to delineate the offshore edge of the plume; also, the third-mode response varies over the spring-neap cycle, suggesting a modulation of the outflow plume by a tidal residual eddy. The analysis therefore has provided a useful, exploratory examination of this dataset of surface currents.

1. Introduction

Shore-based HF Doppler radars measure at high resolution the spatial and temporal evolution of the two-dimensional surface current field over a large coastal domain (e.g. Prandle, 1987; Shay et al., 1995; Graber et al., 1996; Shay et al., 1998). Because of the large data sets created, it is of interest to have a technique that can easily extract principal circulation features and reduce the data set to a more manageable size. A common technique is empirical orthogonal function (EOF)

* Corresponding author. Tel.: 001 202 767 3756; fax: 001 202 767 3303; e-mail: marmorino@nrl.navy.mil.

0278-4343/99/$ - See front matter
PII: S0278-4343(98)00078-8

analysis. An EOF analysis decomposes the data into orthogonal eigenfunctions, or modes, the first several of which generally account for a large part of the data variance and can generally be related to physical phenomena. The structure of the modes (and their time-varying amplitudes) can be used to explore spatial and temporal coherence, to reveal higher-order flow structures, and to provide 'smoothed' versions of the flow field. Investigators typically use the 'rotary' EOF method (Kundu and Allen, 1976) after low-pass filtering the data or removing the tides (e.g. Prandle and Matthews, 1990; Ng, 1993; Tsimplis et al., 1997). In a rotary analysis, the two-dimensional velocity data are represented by complex time coefficients and complex eigenfunctions.

An alternative to the rotary method is a 'real-vector' EOF analysis, which has been used recently by Kaihatu et al. (1998) to analyze a complicated and time-variable flow regime off Cape Hatteras, North Carolina. This approach uses a mathematical formulation which leaves the vector structure of the data set intact and therefore can be readily extended to treat three-dimensional vector data sets. Compared with the rotary method, Kaihatu et al. show that the real-vector method appears to be better at preserving certain properties of the original current fields (such as the horizontal divergence) and seems to separate more cleanly unidirectional from 'eddy-like' flows. Thus the real-vector method may be more useful in delineating persistent fronts and topographically steered flows. The present paper further explores the usefulness of this method by employing it on a new dataset. To make our study as similar as possible to Kaihatu et al.'s, the analysis is performed with no *a priori* bandpass filtering of the observations or removal of the tidal currents. The EOF calculation thus serves as an unbiased analysis of spatial and temporal structure in the data set.

The HF Doppler radar data to be analyzed were collected by the University of Miami as part of a study of the buoyant outflow from the Chesapeake Bay (Fig. 1). Forcing is expected to be by the wind, by predominantly semidiurnal tidal currents (of the order of 0.5 m/s near the bay mouth), and by the buoyant discharge (annual mean of 2500 m^3/s). The behavior of the discharge has been studied by a number of investigators (e.g. Boicourt et al., 1987; Chao, 1988; Chao, 1990; Wheless et al., 1996). The typical response is that water in the discharge plume undergoes a broad, anticyclonic (right-handed) turn upon exiting the mouth of the bay. This 'plume-turning' response is a result of the Coriolis force and of steering by a residual clockwise eddy located south of the mouth, between Cape Henry and Rudee Inlet (Harrison et al., 1964). These flows are sketched in Fig. 1, based largely on the drifter and current measurements of Harrison et al. (1964). The eddy arises from non-linear effects averaged over a tidal cycle, which are predicted to preferentially accumulate negative vorticity to the right of the exit through an estuary mouth (Imasato, 1983; Chao, 1990). Thus the eddy should be present with varying intensity through the lunar month. As shown in the sketch, the plume reattaches to the coast at a location south of Rudee Inlet. Farther downcoast the plume water has been observed to accelerate in a rotationally trapped coastal jet. Under sufficiently strong southerly (upwelling-favorable) winds, the plume is forced to spread seaward through Ekman circulation and so the plume-turning response is weakened and no coastal jet is formed. An objective of this paper is to determine whether the EOF analysis can extract tidal,

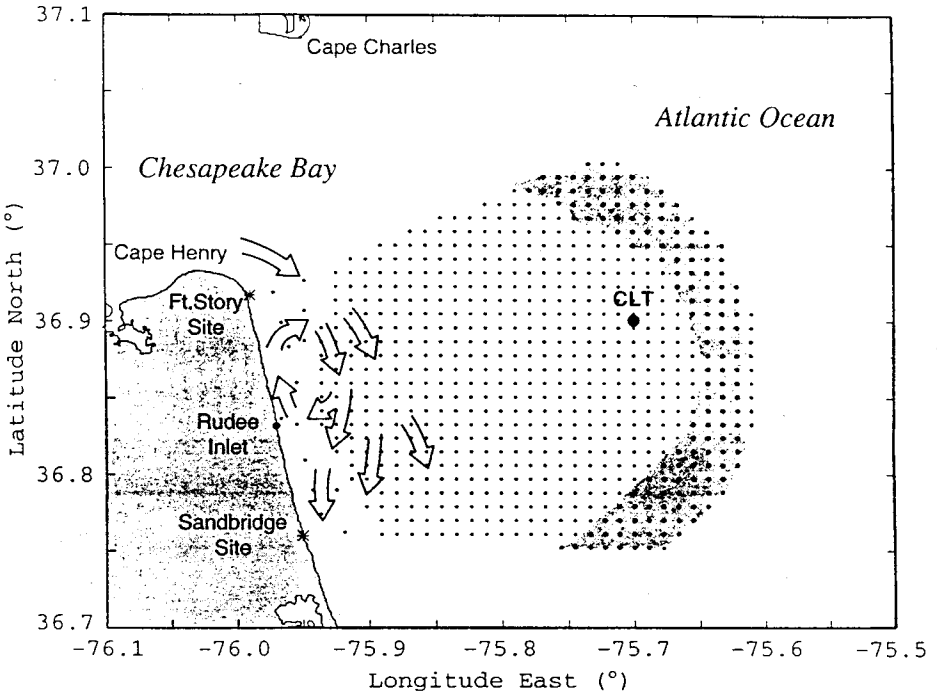

Fig. 1. Study area showing location of HF radar surface current measurement cells (dots). Shaded region shows where vector returns fall below the 85% level. Asterisks show location of radar installations. CLT denotes the Chesapeake Light Tower (36.9°N, 75.7°W). The arrows indicate the non-tidal residual flow based on drifter and current meter measurements.

wind- and buoyancy-driven flows in a way that provides insight about the dynamics and spatial structure of the plume.

2. Field measurements

A Chesapeake Bay outflow plume experiment (COPE-1) was a multi-institutional effort conducted in September 1996. The field program involved several ships and aircraft as well as the shore-based HF radar measurements (which continued through early October) used in this paper.

2.1. Environmental data

While the experiment was planned to measure conditions during the low outflow conditions typical of autumn, tropical storms Bertha and Fran caused dramatically increased streamflow rates. This resulted in a September average streamflow into the bay of 4021 m^3/s, which is 3.6 standard deviations above normal for the month and comparable to normal springtime values. Thus, the results of this study should apply

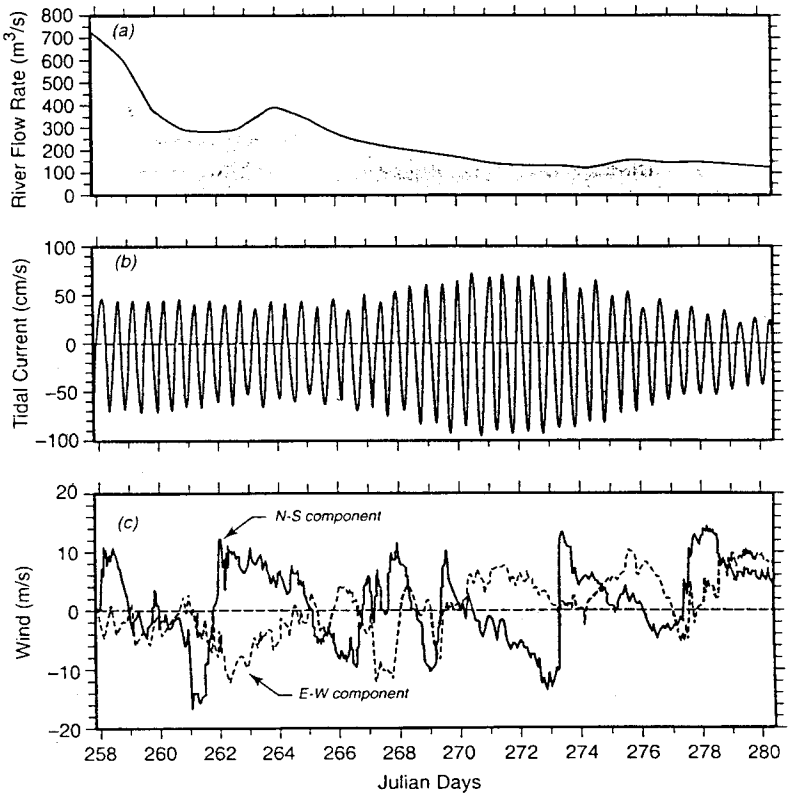

Fig. 2. Environmental data. (a) Streamflow data from James River, located in the southern part of the Chesapeake Bay, computed from an upstream gauging station of the James plus flow in the Appomattox, Canal, and Chickahominy rivers. (Data provided courtesy of USGS.) (b) Predicted current at the bay mouth station (36.98°N, 75.0°W), based on historical observations and model calculations. A positive current is directed toward 302°T, which is the direction of the maximum flood tidal current at this station. (c) Wind measurements made at the Chesapeake light tower.

to periods of maximum plume development. Streamflow data from the southernmost river in the estuary, the James River, are shown in Fig. 2a to illustrate the time variability of the freshwater discharge over the experiment period. As a result of the strong buoyant discharge in September, the water column was strongly stratified. Airborne and *in situ* salinity measurements (Miller, 1998) showed values of about 22 in the plume and 28 to 30 in the ambient shelf water, giving a reduced gravity value of $g' = g\Delta\rho/\rho_{\text{ambient}} \approx 0.057\ \text{m/s}^2$. Also, *in situ* measurements made by the first author suggest a depth of about 5 m for the plume water.

Fig. 2b shows the predicted tidal current at a station in the mouth, northeast of Cape Henry. The current variation is predominantly semi-diurnal, and both a primary and secondary spring tide occur during the period shown. The fortnightly variability in the tidal current results from the interaction among the three semi-diurnal tidal constituents (M_2, N_2, and S_2).

Fig. 2c shows the winds measured during the experiment at the Chesapeake Light Tower (see Fig. 1 for location). For wind speeds greater than about 8 m/s, the wind was from either the southeast or northwest quadrants with the most probable directions being about 180°T and 330°T. Over the shelf, the wind-response of the plume is expected to be mostly through surface Ekman drift effected by along-shelf wind stress (Chao, 1988). For this reason, the results will be compared with the wind component aligned in the north-south direction, which is the approximate mean orientation of the coastline and isobaths.

2.2. *Hf doppler radar dataset*

Doppler radar measurements were made with the University of Miami's ocean surface current radar (OSCR) system operated at HF (25.4 MHz) radio frequency (Haus et al., 1998). OSCR measured surface currents every 20 min from shore sites at the US Army base, Fort Story, Virginia (located just southeast of Cape Henry) and at the US Navy Fleet Combat Training Center Atlantic base near Sandbridge, Virginia, located about 25 km farther south (Fig. 1). The OSCR domain extended about 40 km offshore, with a spacing between cells of about 1.2 km. Vector data were collected over the majority of the domain more than 95% of the time. Data return was affected by power outages from a remote diesel generator and low signal-to-noise at far ranges, where vector returns dropped to as low as 65% at the most distant cells. (The shaded region in Fig. 1 shows where vector returns fall below the 85% level.) Measurement resolution was better than 8 cm/s for north–south velocity over the entire domain and better than 4 cm/s for east–west velocity over the offshore part of the domain; within 5 km of shore the east–west resolution degraded considerably.

The data set analyzed is 22.7 days long (1633 20 min time steps), covering the period 2000 UT 13 September (JD 257.833) to 1200 UT 6 October (JD 280.5). Of these, 173 time steps (11%) were linearly interpolated because of data collection problems, though 90 of these time steps occurred as a single gap on JD 260-261. Results deriving from the interpolated data are not shown.

3. Real-vector EOF method

Though the real-vector EOF method has been used extensively in the study of turbulence (e.g. Lumley, 1967; Sirovich, 1987; Holmes et al., 1996; Webber et al., 1997), its first use with geophysical data was apparently by Kaihatu et al. (1998). Kaihatu et al. (1998) make a detailed comparison of the real-vector and complex EOF methods. Several important differences were noted such as: (1) if the current field is free of divergence, so are the real-vector eigenmodes, whereas the complex eigenmodes are not; (2) the real-vector method can treat a three-dimensional velocity vector, as opposed to the complex method which treats only two velocity components at a time; and (3) the real-vector method appears to separate more 'cleanly' unidirectional from eddy-like flows and so can separate along- and across-shelf dynamics when each is responding to a different forcing, though the complex analysis is able to capture

certain classes of rotary motion in a single mode. Neither of the EOF methods naturally sort data into modes corresponding to distinct forcing mechanisms, but the real-vector approach seems to us the more physically appealing. These considerations lead us to continue to apply the real-vector analysis to the OSCR data sets.

In the real-vector approach, an inner product $(\boldsymbol{u}, \Psi)$ is defined by

$$(\boldsymbol{u}, \Psi) = \int u_j \Psi_j \, \mathrm{d}\boldsymbol{x}, \; (j = 1, 2) \tag{1}$$

where $u_j = (u_1, u_2)$, $u_1 = u$, $u_2 = v$, and repeated indices imply summation, and therefore $u_j \Psi_j$ is simply the dot product of the current field with the eigenmodes. The functions Ψ_j are sought which maximize the variance λ, given by

$$\lambda = \langle (\boldsymbol{u}, \Psi)^2 \rangle = \lim_{T \to \infty} \frac{1}{T} \int_0^T (\boldsymbol{u}, \Psi)^2 \, \mathrm{d}t \tag{2}$$

under the constraint $(\Psi, \Psi) = 1$. In other words, this maximizes in a statistical sense the alignment between the velocity field and the eigenmodes. In Eq. (2) we assume the process is ergodic so that temporal averaging is equivalent to ensemble ($\langle \, \rangle$) averaging. This leads to the eigenvalue problem

$$\int R_{ij}(\boldsymbol{x}, \boldsymbol{x}') \; \Psi_j^{(k)}(\boldsymbol{x}') \, \mathrm{d}\boldsymbol{x}' = \lambda_k \, \Psi_i^{(k)}(\boldsymbol{x}) \tag{3}$$

where $R_{ij}(\boldsymbol{x}, \boldsymbol{x}') = \langle u_i(\boldsymbol{x}) \, u_j(\boldsymbol{x}') \rangle$. The current field can then be expanded in terms of the eigenfunctions as

$$u_i(\boldsymbol{x}, t) = \sum_k a_k(t) \; \Psi_i^{(k)}(\boldsymbol{x}) \tag{4}$$

where $a_k(t) = (\boldsymbol{u}, \Psi)$ contains the time variation of each mode. Note that both a_k and Ψ are real. The eigenvalue problem leads to a complete set of orthonormal eigenfunctions $\Psi_i^{(k)}$, each corresponding to real positive eigenvalues λ_k. See Kaihatu et al. (1998) for details on the numerical implementation of the real-vector method.

We have deleted 14 of the near-shore OSCR cells from the EOF analysis. These had irregular horizontal spacing and large expected errors in the east–west velocity component (because of the radar beam geometry). In addition, although all realizations $u(x, t)$ were included in the analysis, we do not display those time steps in the amplitude series having anomalous spikes resulting from residual errors in the radial velocity. The temporal mean at each measurement cell was subtracted from the time series at each of the cells prior to the EOF analysis.

4. Results

4.1. Mean field

The temporal mean velocity field (Fig. 3) shows a flow that is strong near the mouth of the bay, then weakens in a broad turn to the southeast which resembles the pattern

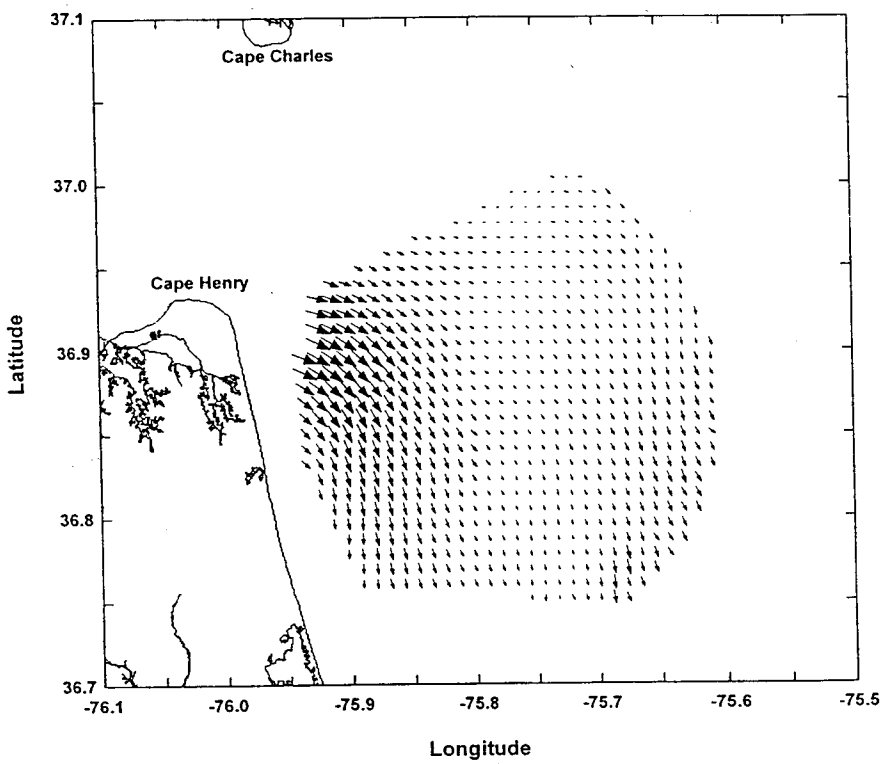

Fig. 3. Temporal mean flow field. The largest vector in the field (occurring near the mouth of the bay) corresponds to a speed of 29.4 cm/s. The increase in speed from the middle of the domain toward the eastern part of the field is believed to be a spurious effect resulting from a decrease in signal-to-noise along the far-range perimeter of the domain.

of the buoyant outflow sketched in Fig. 1. There is no clear manifestation of the residual eddy in the mean field, however. Near the mouth, the mean surface current is about 30 cm/s. Currents are weak in the middle and northern part of the domain. An increase in current speeds in the eastern and southeastern parts is suspect as the signal-to-noise is lower in this region (cf. Fig. 1).

4.2. Modes 1–3

The first three EOF modes together account for 76% of the variance in the dataset (Fig. 4a). Experimentation with subsets of the data suggests that this percentage is a lower bound because of outliers in the data (due to signal-to-noise and other problems). For example, a separate analysis that excluded OSCR cells having vector returns less than 85% showed that modes 1–3 accounted for 82% of the variance. In any of the calculations performed, modes 1–3 were judged to contain the only

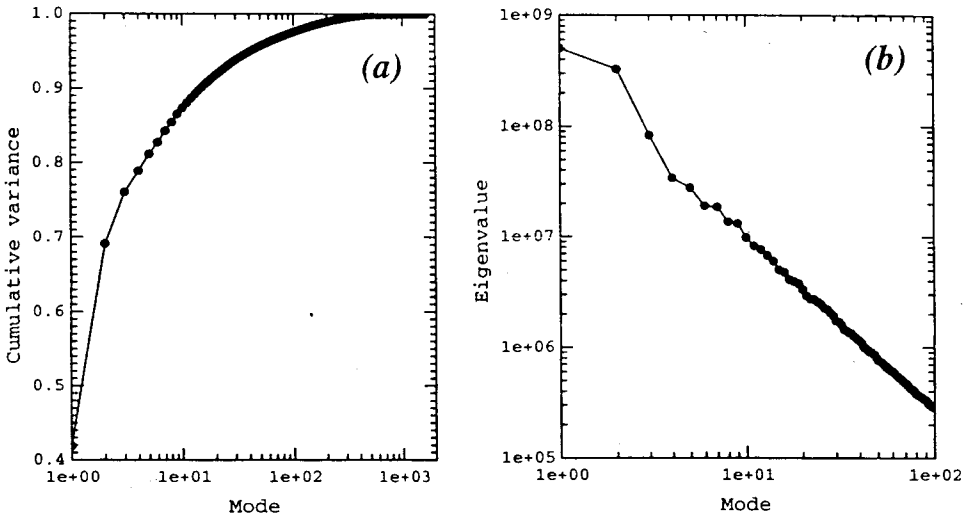

Fig. 4. Cumulative variance (a) and eigenvalue (b) plotted against mode number.

statistically significant results. The evidence for this is that higher modes (out to at least mode 100) fall nearly on a straight line in a log–log plot of variance vs mode number (Fig. 4b), while modes 1–3 lie above the line. The power-law relationship for the higher modes is consistent with the behavior expected for random spatial structure in what is called the 'deep' part of the mode spectrum (Sirovich et al., 1995).

Fig. 5 shows the vector field and amplitude time series for mode 1, which alone accounts for 42% of the variance. The flow field offshore is approximately spatially uniform but near the mouth the flow is stronger and curves inward toward the coast. The time behavior of the amplitude $a(t)$ of mode 1 is shown in the lower part of the figure. Large-amplitude low-frequency signals in $a(t)$ can be seen to correspond closely with the north-south wind component (shown overlain on the $a(t)$ plot). Thus, mode 1 captures the wind-forced flow. North wind events drive a positive mode 1 response (i.e. a southward current) and south winds a negative response. Smaller-amplitude signals of semidiurnal frequency are seen to modulate the larger wind response, but these produce reversals in the flow only when the wind forcing is relatively weak. Some enhancement of the flow occurs inshore near the mouth. This is consistent with the expected stronger tidal currents there and with wind-forced exchange with bay which, because of the large north–south extent of the bay axis, responds preferentially to generally north–south wind forcing (Wang and Elliott, 1978).

The results for mode 2 are shown in Fig. 6. This mode accounts for 27% of the variance. The flow is aligned across shore and so is approximately perpendicular to the mode 1 flow. The amplitude fluctuations are dominated by the semi-diurnal tide and are approximately synchronized with the predicted tidal current (dashed curve in Fig. 6), with a positive mode 2 response corresponding to flood. Larger amplitudes

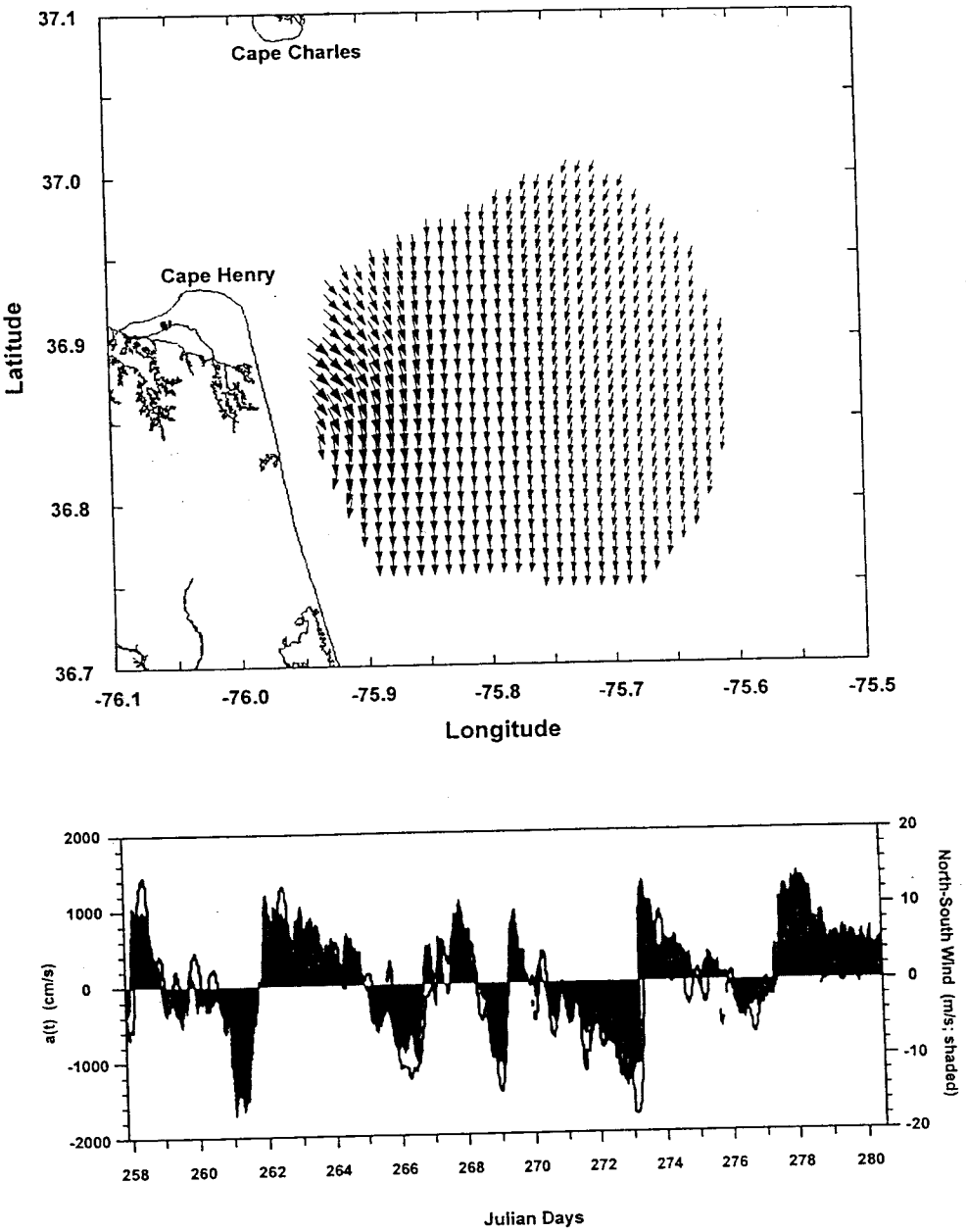

Fig. 5. Mode 1 results. (Top) Vector map and (bottom) amplitude time series $a(t)$. Scale factor for the spatial field is 0.059 (i.e. the relative length of the largest vector). An individual current speed is calculated by multiplying a scaled vector in the map by an $a(t)$ value. Blanks in the $a(t)$ plots show periods of data gaps in the original OSCR data and outliers in the results. The north–south wind is overlain on the $a(t)$ plot as a shaded region and shows a northward-directed airflow, i.e. a south wind, in the positive $a(t)$ direction.

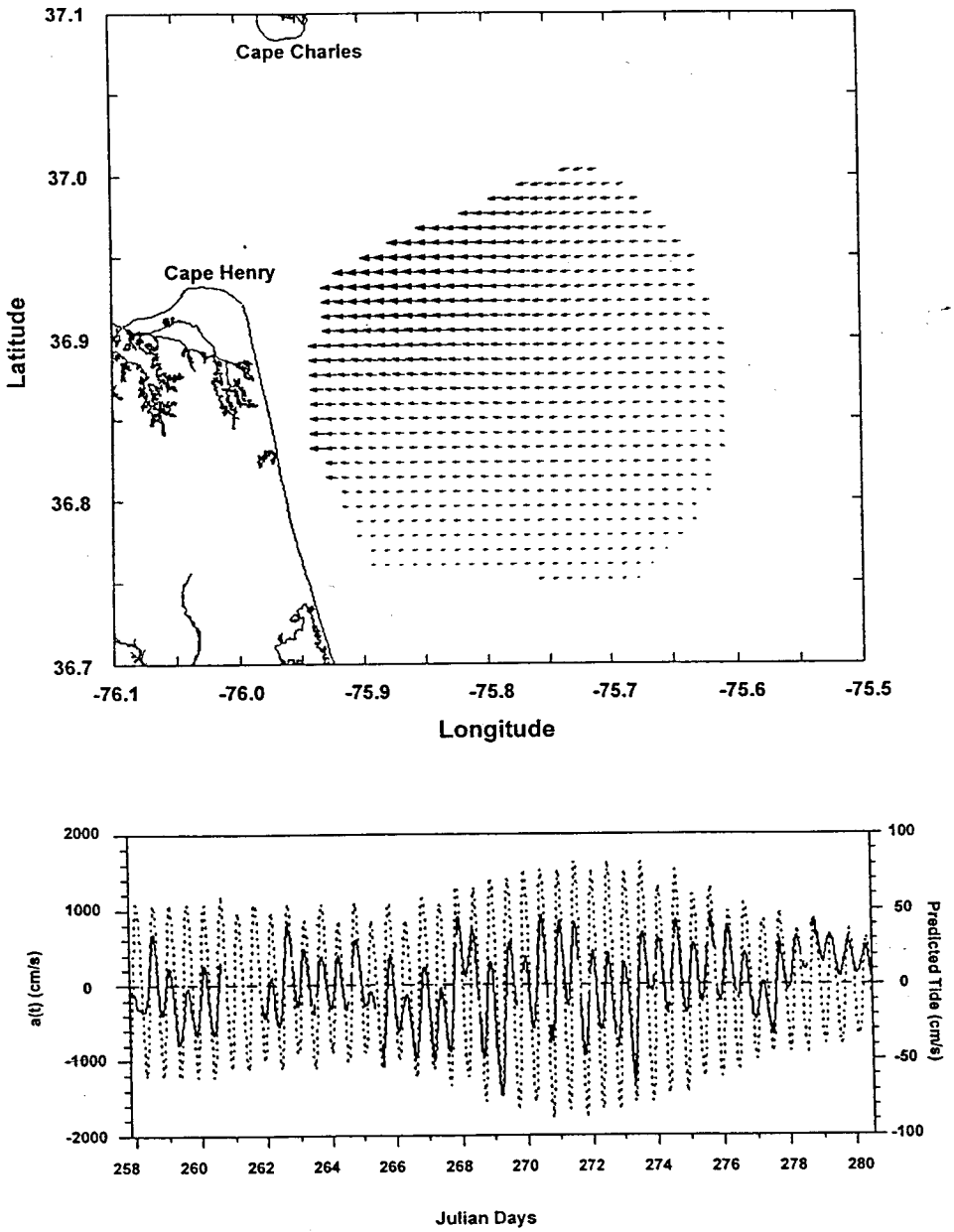

Fig. 6. Mode 2 results. Scale factor for the spatial field is 0.082. Dashed curve shows predicted tidal current in the bay mouth (scale on right-hand axis).

occur over the later half of the record which corresponds to spring tide. Currents near the mouth show a range of about ±80 cm/s (obtained by multiplying the mode-2 scale factor of 0.082 by the range in $a(t)$ values), which is comparable to the predicted range. Because the actual tidal current rotates over time and becomes oriented along-shelf away from the mouth, a (weaker) tidal signal also appears in the mode 1 amplitude series, as noted above.

Results for mode 3 are shown in Fig. 7. In this case, a positive response ($a(t) > 0$) corresponds to a strongly curving downcoast flow separated from a broad offshore region of weaker northwestward flow. This creates a curved nodal region where the flow is approximately zero and across which there is a large-scale shear. The amplitude series for mode 3 shows both an intratidal as well as a longer-period modulation of the flow field. The intratidal response is driven positively during late ebb and early flood. During late ebb stage, the plume discharge is strong relative to the offshore flow and during early flood the buoyant discharge exceeds the flood current but the offshore flow is flooding and so is in opposition (see below). These effects create the region of shear and near-zero relative flow comprising the nodal region, which thus represents an additional but higher-order manifestation of the plume. The long-period oscillation has an amplitude of about 15 cm/s and a period of about 14 days (the solid curve in Fig. 7). The oscillation is approximately in phase with the fortnightly spring-neap cycle; hence, it likely represents a modulation of the basic plume-turning response through the influence of the tidal residual eddy.

4.3. *Flow reconstruction*

While modes 1–3 account for a high percentage of flow variance on a global basis, it is of interest to examine how well they represent an individual flow realization. Therefore, Fig. 8 compares an original OSCR map with a flow field reconstructed from EOF modes 1–3 plus the mean field. The particular time shown (JD 269.94) was chosen because of the availability of a simultaneous radar image showing the position of the convergence front lying along the offshore edge of the plume. Conditions at this time correspond to early flood and calm winds (Fig. 2). The original OSCR map (Fig. 8a) shows a strongly curving nearshore flow and a weaker offshore flow directed to the north and northwest. The reconstructed field (Fig. 8b) shows a generally similar flow field but smoother, as one would expect. The curving region of downcoast flow is consistent with the positive mode 3 response at this time (Fig. 7). The frontal position derived from the radar image (shown in Fig. 8a) delineates the offshore edge of the curving flow. This location also corresponds to the position of the mode 3 nodal line. *In situ* current measurements collected across the front simultaneously with the radar image showed a strong near-surface current shear (and convergence), which is consistent with the (coarser) OSCR measurements. These current gradients, which were intensified during the early flood, created strong wave–current interactions along the front, making it detectable by the radar.

There are of course differences between the original OSCR map and the reconstructed field (Fig. 8c). Some of these differences arise from spurious data; for example, close examination of Fig. 8 shows some vectors having anomalous directions or speeds

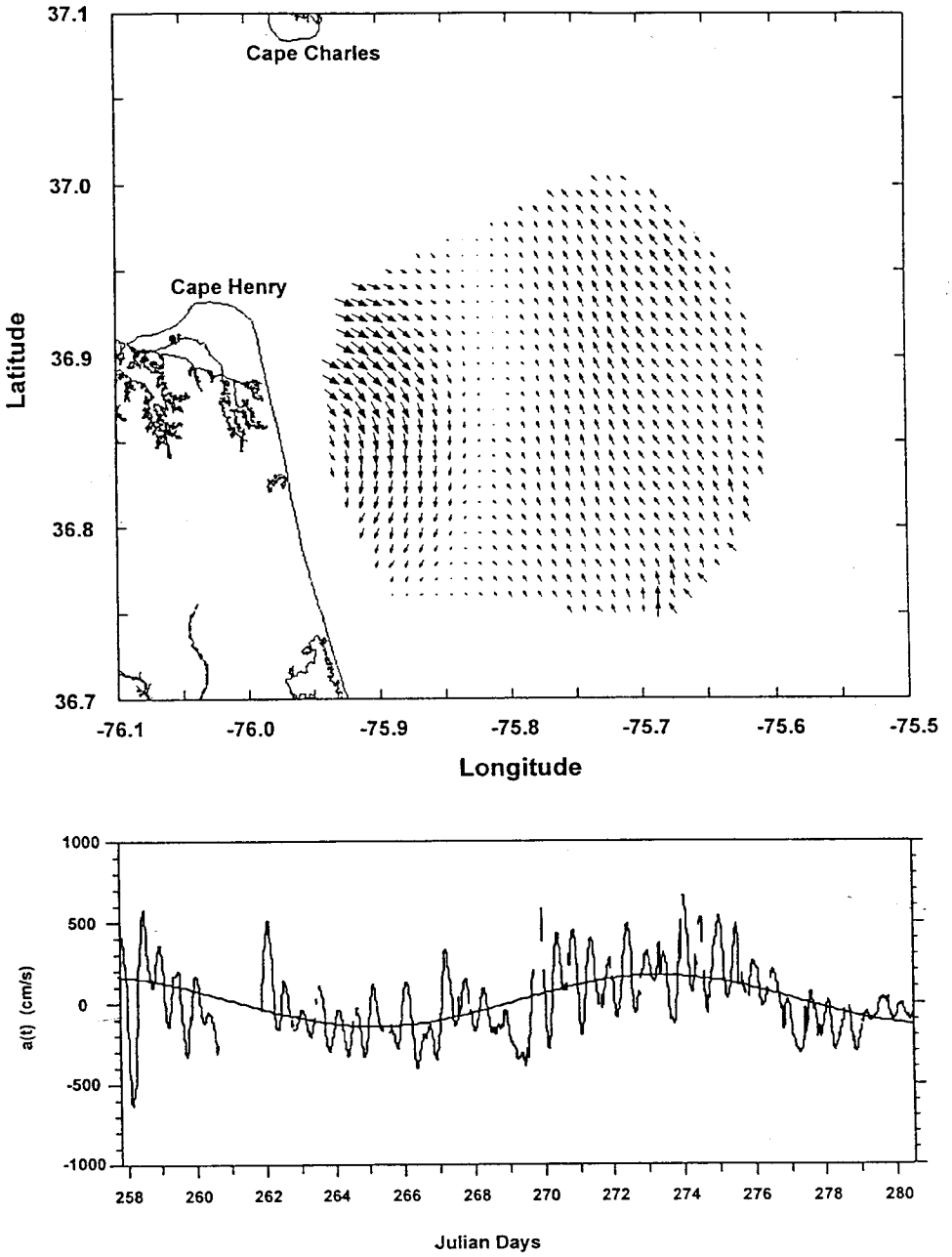

Fig. 7. Mode 3 results. Scale factor for the spatial field is 0.080. ~~Dashed curve shows predicted tidal current~~. Solid curve shows best-fit sinusoidal (period of 14.3 days), covering only days 262–280, i.e. just the period after the data gap on 260–261. A fit over the entire interval (days 258–280) has a period of 16.3 days.

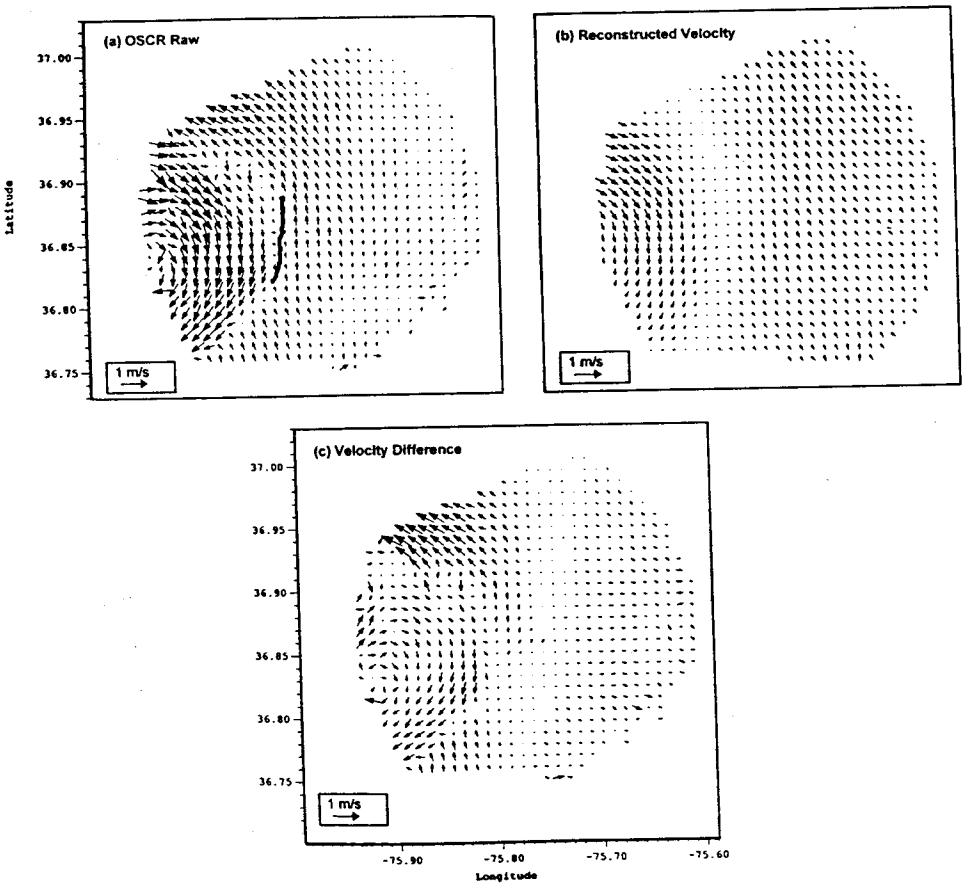

Fig. 8. An original surface current map (a), a reconstructed flow field (b), and the difference between them (c). The reconstructed field uses EOF modes 1–3 plus the mean field. The time of the maps is JD 269.944 (25 Sep 2240 UT). The line segment in (a) shows the position of the offshore edge of the plume at 2216 UT as measured by an airborne radar. The position of plume front corresponds approximately with the nodal line in the mode 3 spatial map. (Frontal position courtesy of M. Sletten and T. Donato, NRL.)

when compared with neighboring vectors, suggesting random spatial errors in the data. Other, more spatially regular, discrepancies arise from not using all the EOF modes in the reconstruction. For example, a relatively strong flow toward the mouth near 36.95°N and a tight, circular flow at 36.83°N (which resembles the eddy sketched in Fig. 1) are not captured well by using only modes 1–3, but they do resemble structure in the higher modes, which obviously do contribute at times to the total flow field. Comparisons made for time periods other than the one shown also show a close approximation of the original flow pattern with significant differences generally confined mostly to the onshore flow component nearest the coast where measurement errors are higher.

Given that modes 1–3 capture the dominant flow patterns, the reconstructed flow field through one complete tidal cycle is shown in Fig. 9. Winds over this period were from the north at about 5 m/s. Panel (a) shows the flow near predicted high-water slack. The flow is weak inshore but increases offshore due to wind forcing. Conditions during ebb (panels b–e) and flood (f–i) show the interplay of primarily modes 1 and 2. Conditions during flood appear to show more spatial variability than during ebb. The amplitude of mode 3 is weaker over this period than for the case in Fig. 8 and so its

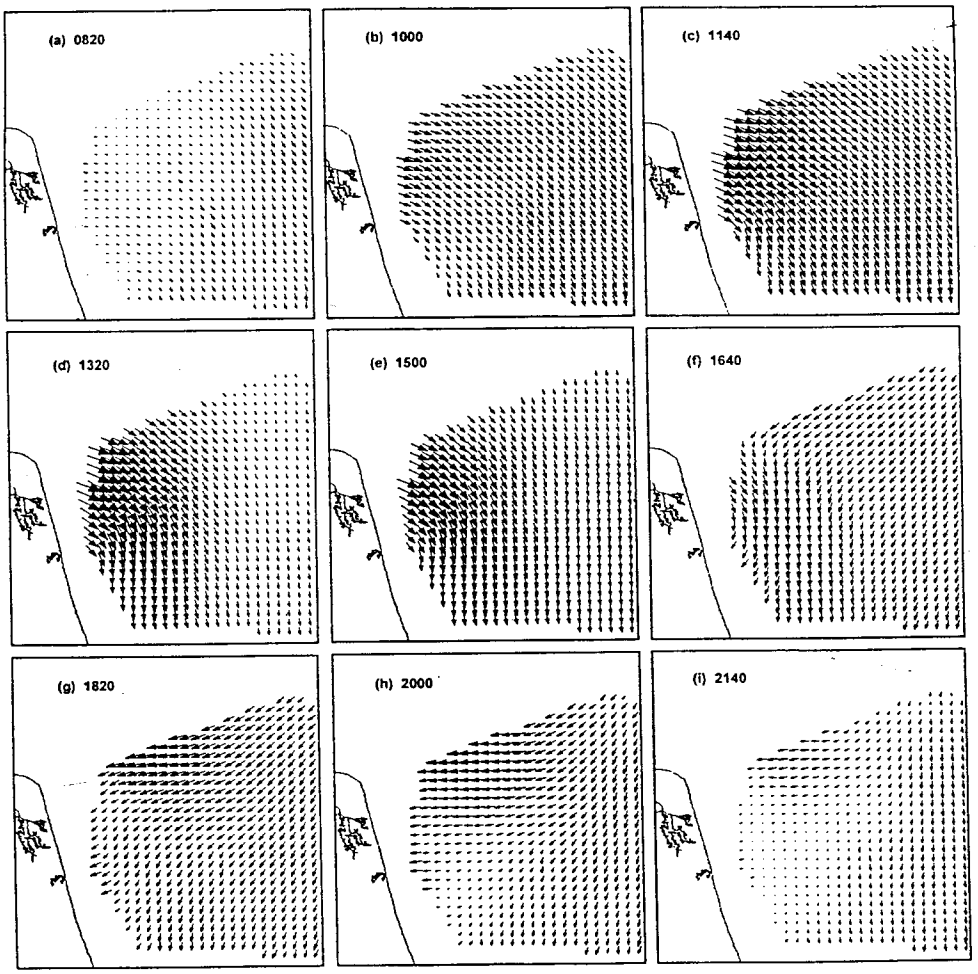

Fig. 9. Reconstructed flow over a complete tidal cycle on JD 264 (20 Sep) 0820-2140 UT. The flow fields (a–h) are shown at intervals of 1 h 40 min; for clarity, only the western two-thirds of the study domain is shown. The reconstruction uses the sum of the mean field and EOF modes 1–3. A fixed velocity scale length is used for all the fields. The longest vectors (which occur in panel d) correspond to a current of 70 cm/s. The field in panel (d) is based on an interpolation of the modal amplitudes. Based on the predicted tide at the mouth, slack occurs at 0832, 1534, and 2201 UT. Panels (b–e) represent ebb conditions, panels (f–i) flood.

contribution is not so apparent in the flow patterns in Fig. 9. Note that, because of a data gap from 1240-1440 UT, the map at 1320 UT (Fig. 9d) has been reconstructed using interpolated values; however, the values shown derive from interpolated mode 1–3 amplitudes as this gave a more realistic-appearing flow field than using the amplitudes based on the interpolated data.

5. Summary and discussion

An EOF analysis has been presented of surface currents measured by the University of Miami's OSCR HF Doppler radar system in the region of the Chesapeake Bay outflow plume during strong buoyancy forcing (typical of spring conditions). The 'real-vector' empirical orthogonal function (EOF) analysis (Kaihatu et al., 1998) was used on the full data set (no a priori bandpass filtering or removal of the tides) after first removing the temporal mean field which contains the broadly curving buoyant outflow from the bay. The analysis shows that the first three EOF modes account for 76% of the variance in the data set. Separate analysis of subsets of the data (having the far-range areas of lower signal-to-noise deleted) show that the first three modes account for 82% of the variance. Therefore, as a data-compression technique, the analysis has worked relatively well.

The analysis has also provided insight into the dynamics and spatial structure of the plume. For example, mode 1 shows a clear correlation with the wind and so has extracted most of the wind-forced surface flow. Mode 2 extracts the across-shelf component of the semi-diurnal tidal flow, which is dominant nearer the mouth of the bay. A weaker along-shelf tidal signal appears in mode 1 in addition to the wind response as two real-vector modes are needed to capture a rotary tidal current.

The spatial structure of mode 3 is shown to contain a curved region of horizontal shear and weak relative flow that appears to delineate the offshore edge of the plume. The width of the curved nodal region is larger than the front would appear in a single realization, of course, because the mode 3 spatial field represents a temporal average. Thus it includes smearing through the effects of frontal propagation, variable wind forcing, and varying strength of the tide. The amplitude of mode 3 varies intratidally, reflecting the modulation of the velocity gradient across the plume-shelf water front. As the amplitude achieves a local maximum at the transition from ebb to flood, we expect the front should be well established then, too. This would be consistent with previous studies which show that the frontal convergence is largest at late ebb-early flood when the most low-density water is on the shelf (e.g. Sanders and Garvine, 1996) and when the offshore tidal current opposes the buoyant outflow (Kalponai et al., 1996; Wheless and Valle-Levinson, 1996). A fortnightly oscillation in the strength of the mode 3 amplitude was found, as well. We explain this as a modulation of the basic plume-turning mechanism by a variation in strength of the residual tidal eddy, which appears to have an amplitude of the order of 15 cm/s. Stronger tidal forcing would lead to a stronger residual eddy that can steer the basic plume flow. Thus the tide and low-frequency flows are non-linearly coupled; hence, we predict that structure similar to that of the present mode 3 should still appear in an analysis of a 'detided' data set.

The structure of the eddy might be better resolved in a separate study that uses all the available inshore OSCR cells.

The location of the mode 3 nodal line as well the pattern of the mean flow field shown in Fig. 3 suggest that on average the plume flow reattaches to the coast near 36.75°N. This is consistent with the reattachment position sketched in Fig. 1 and which occurs south of Rudee Inlet (36.83°N). Based on the mode 3 flow field, the plume appears to having a turning radius of about 15 km as measured from Rudee Inlet. An estimate of the (baroclinic) Rossby radius $R_o = (g'h')^{1/2}/f$ is of the order of 5 km, where $h' = h(H - h)/H$, $h \approx 5$ m is the estimated plume thickness in the exit region of the mouth, $H \approx 16$ m is the water depth in the mouth, and $f = 8.76 \times 10^{-5}\,s^{-1}$ is the Coriolis parameter. Therefore, the plume turning radius is equal to about 3 Rossby radii. This is consistent with Yankovsky and Chapman's (1997) prediction that, under strongly stratified conditions when the plume is confined to the surface (such as in this study), the turning radius is predicted to be a *minimum* of two Rossby radii.

These results provide an interesting contrast to those of Kaihatu et al. (1997). Their study area was the narrow shelf region near Cape Hatteras, NC, located about 170 km south of the Chesapeake Bay mouth. (They used the same University of Miami OSCR system as in the present study.) That area is subject to multiple influences such open-ocean forcing from the Gulf Stream and intrusion of buoyant coastal water masses, including the plume water from the Chesapeake Bay. This led to flow structures over the shelf that were spatially complex and highly variable in time. As a result, when their data were analyzed as in the present paper (i.e. with no pre-filtering and with the mean removed) the 'convergence' of the EOF analysis was found to be relatively slow in that the first ten modes captured only 74% of the flow variance. (Modes 1–10 are significant in their results based on the same criterion as applied to our Fig. 4.) Because the flow regime associated with the outflow plume exhibits greater persistence and repeatability in structural details, fewer modes should be needed to account for the same level of variance. Indeed, this is what was found in the present paper, modes 1–3 accounting for 76% of the variance.

We conclude that this analysis has provided a useful examination of spatial and temporal structure in the data, and was fairly successful at extracting meaningful flow patterns in three significant EOF modes. That we did not first low-pass filter the data or remove the tidal components insured that the analysis was unbiased (though our interpretations of the results, being necessarily somewhat subjective, may not be so unbiased); however, a similar analysis could of course be done on the filtered data sets. For these reasons, this work should be viewed as exploratory in nature and our interpretations of the results should be tested in additional studies.

Acknowledgements

This research was supported by the Office of Naval Research. Work at NRL was done as part of the Physics of Coastal Remote Sensing Accelerated Research Initiative, which is managed at NRL by Richard Mied. RSMAS investigators were

supported by ONR Contract N00014-96-1-1065. The continued support of the RSMAS OSCR system by the ONR Remote Sensing Research Program through grants N00014-96-1065 (Graber, Shay, and Haus) and N00014-96-1-1011 (Shay) is appreciated. J. Martinez, Mike Rebozo, and T. Faber helped conduct the field phase of the OSCR operations. Streamflow data were kindly provided by Mr. G.T. Fisher of the Baltimore, MD office of the U.S. Geological Survey. Comments from Dr. Carl Friedrichs and an anonymous reviewer were helpful in revising the manuscript.

References

Boicourt, W.C., Chao, S.-Y., Ducklow, H.W., Glibert, P.M., Malone, T.C., Roman, M., Sanford, L.P., Fuhrman, J., Garside, C., Garvine, R., 1987. Physics and microbial ecology of a buoyant estuarine plume on the continental shelf. Eos. 69, 666–668.

Chao, S.-Y., 1988. Wind-driven motion of estuarine plumes. Journal of Physical Oceanography 18, 1144–1166.

Chao, S.-Y., 1990. Tidal modulation of estuarine plumes. Journal of Physical Oceanography 20, 1115–1123.

Graber, H.C., Thompson, D.R., Carande, R.E., 1996. Ocean surface features and currents measured with SAR interferometry and HF radar. Journal of Geophysical Research 101, 25,813–25,832.

Harrison, W., Brehmer, M.L., Stone, R.B., 1964. Nearshore tidal and non-tidal currents, Virginia Beach, Virginia. U.S. Army Coastal Engineering Research Center, Tech. Memo. No. 5, 20 pp.

Haus, B.K., Graber, H.C., Shay, L.K., 1998. Ocean surface current observations with HF Doppler radar during the Chesapeake Outflow Plume Experiment, Tech. Rept, RSMAS, Univ. Miami, Miami FL 33149, 66 pp.

Holmes, P.J., Lumley, J.L., Berkooz, G., 1996. Turbulence, Coherent Structures, Dynamical Systems and Symmetry. Monographs on Mechanics, Cambridge Univ. Press, Cambridge, 438 pp.

Imasato, N., 1983. What is tide-induced residual current? Journal of Physical Oceanography 13, 1307–1317.

Kaihatu, J.M., Handler, R.A., Marmorino, G.O., Shay, L.K., 1998. Empirical orthogonal function analysis of ocean surface currents using complex and real-vector methods. Journal of Atmospheric and Oceanic Technology 15, 927–941.

Kapolnai, A., Werner, F.E., Blanton, J.O., 1996. Circulation, mixing, and exchange processes in the vicinity of tidal inlets: a numericl study. Journal of Geophysical Research 101, 14,253–14,268.

Kundu, P.K., Allen, J.S., 1976. Some three-dimensional characteristics of low-frequency current fluctuations near the Oregon coast. Journal of Physical Oceanography 6, 181–199.

Miller, J., 1998. Remote sensing of salinity in the coastal zone. Eos Transactions American Geophysical Union 79, 173.

Ng, B., 1993. The prediction of nearshore wind-induced surface currents from wind velocity measured at nearby land stations. Journal of Physical Oceanography 23, 1609–1617.

Prandle, D., 1987. The fine-structure of nearshore tidal and residual circulations revealed by H.F. radar surface current measurements. Journal of Physical Oceanography 17, 231–245.

Prandle, D., Matthews, J., 1990. The dynamics of nearshore surface currents generated by tides, wind and horizontal density gradients. Continental Shelf Research 10, 665–681.

Sanders, T.M., Garvine, R.W., 1996. Frontal observations of the Delaware Coastal Current source region. Continental Shelf Research 16, 1009–1021.

Shay, L.K., Graber, H.C., Ross, D.B., Chapman, R.D., 1995. Mesoscale ocean surface current structure detected by high-frequency radar, Journal of Atmospheric and Oceanic Technology 12, 881–900.

Shay, L.K., Lentz, S.J., Graber, H.C., Haus, B.K., 1998. Current structure variations detected by HF radar and vector measuring current meters, Journal of Atmospheric and Oceanic Technology 15, 237–256.

Sirovich, L., Everson, R., Manin, D., 1995. Turbulence spectrum of the Earth's ozone field. Physical Review Letters 74, 2611–2614.

Tsimplis, M.N., Velegrakis, A.F., Theocharis, A., Collins, M.B., et al., 1997. Low-frequency current variability at the Straits of Crete, eastern Mediterranean, Journal of Geophysical Research 102, 25,005–25,020.

Wang, D.-P., Elliott, A.J., 1978. Non-tidal variability in the Chesapeake Bay and Potomac River: evidence for non-local forcing. Journal of Physical Oceanography 8, 225–232.

Webber, G.A., Handler, R.A., Sirovich, L., 1997. The Karhunen–Loeve decomposition of minimal channel flow. Physics of Fluids 9, 1054–1066.

Wheless, G.H., Valle-Levinson, A., 1996. A modeling study of tidally driven estuarine exchange through a narrow inlet onto a sloping shelf. Journal of Geophysical Research 101, 25,675–25,687.

Wheless, G.H., Lascara, C.M., Valle-Levinson, A., Brutzman, D.P., Sherman, W., Hibbard, W.L., Paul, B.E., 1996. The Chesapeake Bay virtual environment (CBVE): initial results from the prototypical system. International Journal of Supercomputer Applications and High Performance Computing 10, 199–210.

Yankovsky, A.E., Chapman, D.C., 1997. A simple theory for the fate of buoyant coastal discharges. Journal of Physical Oceanography 27, 1386–1401, 1997.